Fundamentally fastest optical processes at the surface of a topological insulator

S. Azar Oliaei Motlagh, Jhih-Sheng Wu, Vadym Apalkov, and Mark I. Stockman
Center for Nano-Optics (CeNO) and Department of Physics and Astronomy, Georgia State University, Atlanta, Georgia 30303, USA

(Received 19 April 2018; revised manuscript received 19 July 2018; published 17 September 2018)

We predict that a single oscillation of a strong optical pulse can significantly populate the surface conduction band of a three-dimensional topological insulator, Bi_2Se_3. Both linearly- and circularly-polarized pulses generate chiral textures of interference fringes of population in the surface Brillouin zones. These fringes constitute a self-referenced electron hologram carrying information on the topology of the surface Bloch bands, in particular, on the effect of the warping term of the low-energy Hamiltonian. These electron-interference phenomena are in sharp contrast to graphene where there are no chiral textures for a linearly-polarized pulse and no interference fringes for circularly-polarized pulse. These predicted reciprocal space electron-population textures can be measured experimentally by time resolved angle resolved photoelectron spectroscopy (TR-ARPES) to gain direct access to non-Abelian Berry curvature at topological insulator surfaces.

DOI: 10.1103/PhysRevB.98.125410

I. INTRODUCTION

Topological insulators (TI's) represent a modern class of crystalline materials where the bulk is semiconducting and the surfaces are semimetallic [1–4]. The Γ point of the surface-state band is a Dirac point where the electron dispersion is gapless and linear as characteristic of Dirac fermions. In a good approximation, there is locking of spin and linear momentum caused by a strong spin-orbit interaction. This provides protection against backscattering and Anderson localization. The absence of the band gap and, consequently, the linear electron dispersion at the Γ point, are protected by time-reversal ($\mathcal{T}$) symmetry. The Bloch bands near the Dirac point are chiral and carry the Berry phase of $\pm\pi$.

To resolve chirality of the surface states of TI's and related spin textures one has to use a chiral probe: circularly polarized excitation radiation [5–7] or detection of the spin state of electrons in spin resolved angle resolved photoemission spectroscopy (SR-ARPES) [2]. A unique property of the surface bands of a TI—band-dependent locking of the spin and momentum—allows one to manipulate the spin states by controlling the electron momentum in the Bloch bands. Keeping in mind both fundamental interest and spintronics applications, it is important to perform such manipulation as fast as possible, that is within a single optical cycle. Such ultrafast manipulation would allow avoiding significant relaxation, including quantum decoherence during the excitation cycle. It also would open up unique possibilities for ultrafast, PHz-band scale, information processing. Note that the existing experiments on TI's employed relatively long ($\gtrsim$100 fs) excitation pulses of moderate field amplitudes [6], $F_0 \lesssim 10^{-3}$ V/Å. There have been also time-resolved experiments [8–10] on graphene and transition metal dichalcogenides with ultrafast pulses as short as 15–30 fs. These are still much longer than the times on the order of a single optical period that are the aim of this paper.

The goal of this paper is to theoretically show for a three-dimensional (3D) TI a possibility to manipulate electron population, crystal momentum, and consequently spin, in a fundamentally fastest way—during only single cycle of a chiral optical pulse with a moderately strong optical field, $F_0 \sim 0.05$–0.2 V/Å (see field estimates at the end of this section). We have predicted such ultrafast processes earlier for graphene both for linear polarization [11] and circular polarization [12,13]. Electrical currents and charge transfer associated with ultrafast strong-field excitation of graphene have been recently observed experimentally [14]. The underlying chiral distributions of excited electrons in the full Brillouin zone in both the conduction band (CB) and valence band (VB) can fundamentally be observed using time resolved ARPES (TR-ARPES) [8,15–17]. However, such studies have not yet been done.

We predict that, similar to graphene, a significant CB population is induced during a single optical oscillation. The main mechanism responsible for this process is Bloch motion of electrons in reciprocal space induced by strong optical fields. In contrast to graphene, the resulting electron CB distribution in the reciprocal space is highly anisotropic and chiral; to a significant degree it is defined by the so-called warping terms in the effective Hamiltonian [18]. The electron relaxation, which follows the excitation pulse, will cause surface currents and generation of THz radiation. The latter also provides an access to the initial CB electron distribution [19]. Yet another approach to get access to the electron distribution of the surface CB in TIs is ultrafast time-resolved transient reflectivity and Kerr rotation [20].

Specifically, in this work, we study ultrafast electron dynamics on the surfaces of a 3D TI Bi_2Se_3, which has a bulk band gap of ≈ 0.3 eV and gapless surface states [18,21,22]. These gapless surface states are protected by the time reversal symmetry and possess a single Dirac cone located at the Γ point in the reciprocal space [18,23,23,24]. Similar to graphene, the interband dipole coupling at the surface of 3D TI is singular at the Dirac point, and the energy dispersion near the Dirac point is linear (quasirelativistic). The main difference from graphene is that the effective low-energy Hamiltonian in 3D TI's has large nonlinear (cubic) terms. Such terms, which are known as the warping terms, reduce

the point symmetry of the system to threefold (C_3) [18]. This lower symmetry results in unique features in the ultrafast electron dynamics. In particular, as we show below in this paper, for a single-oscillation circularly-polarized pulse, the CB population distribution in the reciprocal space shows a pronounced chirality and a pattern of interference fringes.

Because surface Bloch bands of a TI are gapless, the processes of the electron transfer between the valence band (VB) and CB is nonresonant and, consequently, broadband. Therefore, the dependence on the mean (carrier) frequency or duration of the pulse is very smooth. As an example we choose a pulse with duration of 5 fs (mean carrier frequency $\bar{\omega} \approx 1.2$ eV/$\hbar$). This duration is chosen to be shorter than the fastest electron scattering time [19] in TI's, which is $\gtrsim$10 fs. The pulse electric field causes electron motion in the reciprocal space within each band where the crystal momentum excursion is defined by the Bloch acceleration theorem—see Eq. (7) below. The VB $\rightarrow$ CB transitions occur when an electron passes in a vicinity of the Dirac point (Γ point) or other points where the interband transition dipole matrix element is enhanced. The excursion of electron crystal momentum during the pulse can be estimated as $\Delta k \sim \pi e F_0/(\hbar\bar{\omega})$, where e is electron charge and F_0 is the field amplitude. To travel a half of the Brillouin zone, this excursion should be $\Delta k \sim \pi/a$, where a is a lattice constant. Assuming $a \approx 4$ Å, we obtain $F_0 \approx \hbar\bar{\omega}/(ea) \approx 0.2$ V/Å. Correspondingly, we consider a field amplitude range that includes this value, $F_0 =$ 0.05–0.5 V/Å.

The paper is organized as follows. In Sec. II, a model and main equations, which are used to calculate the electron dynamics in the presence of ultrafast external electric fields, are introduced. In Sec. III, the results for linearly and circularly polarized pulses are presented and discussed.

II. MODEL AND MAIN EQUATIONS

An effective low-energy surface Hamiltonian of Bi_2Se_3 near the Dirac point has the following form [18]

$$H_0 = A_1 k^2 + A_2(\sigma_x k_y - \sigma_y k_x) + A_3(k_+^3 + k_-^3)\sigma_z, \qquad (1)$$

where σ_x, σ_y, and σ_z are Pauli matrices, (k_x, k_y) is crystal momentum, $k_\pm = k_x \pm i k_y = k e^{\pm i\theta}$, $k = (k_x^2 + k_y^2)^{1/2}$, and A_1, A_2, and A_3 are constants that are equal to 23.725 eV Å^2, 3.297 eVÅ, and 25.045 eV Å^3, respectively. The cubic term in this low-energy Hamiltonian leads to a sixth-order warping of the band energy surfaces [cf. Fig. 1 below] and, therefore, is called the hexagonal warping term [25]. The energies of the VB and the CB can be found from the above Hamiltonian as

$$E_c(\mathbf{k}) = A_1 k^2 + \sqrt{A_2^2 k^2 + 4A_3^2 k_x^2 \left(k_x^2 - 3k_y^2\right)^2}\ ,$$
$$E_v(\mathbf{k}) = A_1 k^2 - \sqrt{A_2^2 k^2 + 4A_3^2 k_x^2 \left(k_x^2 - 3k_y^2\right)^2}\ , \qquad (2)$$

where indices c and v stand for the CB and VB, respectively. Near the Γ point (for $k \rightarrow 0$), this dispersion simplifies to two Dirac cones: $E_{c,v} = \pm A_2 k$. This energy dispersion is displayed in Fig. 1 where the Γ point is at $\mathbf{k} = (0, 0)$. Below we assume that the system is undoped, with the Fermi energy at 0, where the VB is fully occupied and the CB is completely empty. This energy dispersion has sixfold symmetry [see Fig. 1(b)], which is due to the warping term.

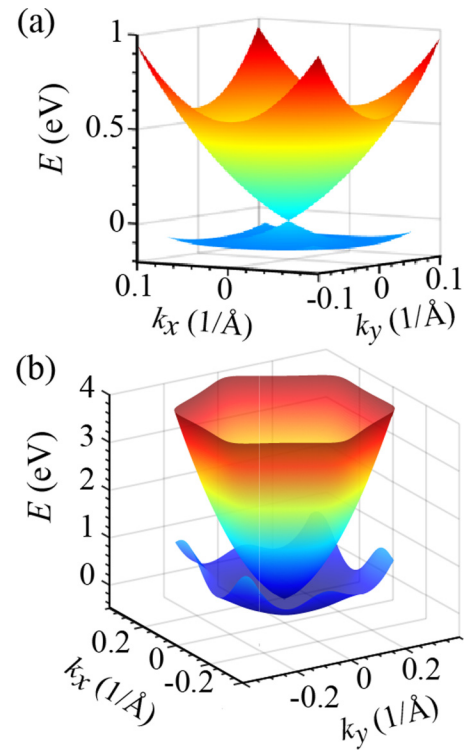

FIG. 1. (a) Low-energy electron dispersion of the surface state around the Dirac point, i.e., the Γ point at $\mathbf{k} = (0, 0)$, as a function of wave vector $\mathbf{k}$. The Dirac cone at the Gamma point is clearly visible. (b) Energy dispersion in a wide range where the sixth-order warping is manifest.

As we have already argued above in Sec. I, during an ultrashort optical pulse with the duration of ~5 fs, electron dynamics is coherent since the electron scattering times in Bi_2Se_3 are $\gtrsim$20 fs. Then the evolution of the system can be described by the time-dependent Schrödinger equation (TDSE),

$$i\hbar\frac{d\Psi}{dt} = H(t)\Psi, \qquad (3)$$

with Hamiltonian

$$H(t) = H_0 - e\mathbf{F}(t)\mathbf{r}, \qquad (4)$$

where $\mathbf{F}(t)$ is the pulse's electric field.

We will be employing moderately intense fields with amplitude $F_0 \gtrsim 0.1$ V/Å. At such intensities, the number of photons, N_p, per pulse within the minimum coherence area of ~λ^2, where $\lambda \sim 1$ μm is wavelength,

$$N_p \sim \frac{c\tau_p \lambda^2 F_0^2}{4\pi\hbar\bar{\omega}} \sim 5 \times 10^7\ , \qquad (5)$$

where c is speed of light; we assume realistic parameters: $\tau_p \sim 3$ fs is the pulse duration, and $\hbar\bar{\omega} \sim 1$ eV is the mean photon energy. With such a large photon number involved, it is legitimate to describe $\mathbf{F}(t)$ as a classical electric field keeping quantum-mechanical description of the solid. This is a usual approach in high-field optics—see, e.g., Refs. [26–28].

Note that quantized optical fields are used for much lower intensities [29,30]. Such a full quantum mechanical approach is not needed for the fields of the amplitude we consider. Instead, we employ the conventional semiclassical approach where the optical field, $\mathbf{F}(t)$, is considered as classical but the underlying solid is treated fully quantum mechanically. We solve the Schrödinger equation in the truncated Houston basis numerically without further approximations. Our pulse is just a single optical oscillation; therefore field $\mathbf{F}(t)$ is not periodic, and its effect cannot be described as band gap modification as in Refs. [29,31]. However, the dynamic Stark effect and other field-dressing effects during the pulse are indeed fully taken into account by our solution.

In solids, the applied electric field generates both the intraband and interband electron dynamics. The intraband dynamics is determined by the Bloch acceleration theorem [32] for time evolution of the crystal momentum $\mathbf{k}$,

$$\hbar\frac{d\mathbf{k}}{dt} = e\mathbf{F}(t). \tag{6}$$

From this, for an electron with an initial crystal momentum $\mathbf{q}$, time-dependent crystal momentum $\mathbf{k}(\mathbf{q}, t)$ is expressed as

$$\mathbf{k}(\mathbf{q}, t) = \mathbf{q} + \frac{e}{\hbar}\int_{-\infty}^{t}\mathbf{F}(t')dt'. \tag{7}$$

The corresponding wave functions, which are solutions of the Schrödinger equation (3) within a single band α, i.e., without interband coupling, are the well-known Houston functions [33],

$$\Phi^{(H)}_{\alpha\mathbf{q}}(\mathbf{r}, t) = \Psi^{(\alpha)}_{\mathbf{k}(\mathbf{q},t)}(\mathbf{r})e^{-\frac{i}{\hbar}\int_{-\infty}^{t}dt_1 E_\alpha[\mathbf{k}(\mathbf{q},t_1)]}, \tag{8}$$

where $\alpha = v, c$ for the VB and CB, correspondingly, and $\Psi^{(\alpha)}_{\mathbf{k}}$ are Bloch-band eigenfunctions in the absence of the pulse field, and $E_\alpha(\mathbf{k})$ are the corresponding eigenenergies.

The interband electron dynamics is determined by the solution of the TDSE (3). Such a solution can be expanded in the basis of the Houston functions $\Phi^{(H)}_{\alpha\mathbf{q}}(\mathbf{r}, t)$,

$$\Psi_{\mathbf{q}}(\mathbf{r}, t) = \sum_{\alpha=c,v}\beta_{\alpha\mathbf{q}}(t)\Phi^{(H)}_{\alpha\mathbf{q}}(\mathbf{r}, t), \tag{9}$$

where $\beta_{\alpha\mathbf{q}}(t)$ are expansion coefficients.

Let us introduce the following quantities

$$\mathcal{D}_{cv}(\mathbf{q}, t) = \mathcal{A}_{cv}[\mathbf{k}(\mathbf{q}, t)]\exp\left(i\phi^{(\mathrm{d})}_{cv}(\mathbf{q}, t)\right), \tag{10}$$

$$\phi^{(\mathrm{d})}_{cv}(\mathbf{q}, t) = \frac{1}{\hbar}\int_{-\infty}^{t}dt'(E_c[\mathbf{k}(\mathbf{q}, t')] - E_v[\mathbf{k}(\mathbf{q}, t')]), \tag{11}$$

$$\mathcal{A}_{cv}(\mathbf{q}) = \left\langle\Psi^{(c)}_{\mathbf{q}}\middle|i\frac{\partial}{\partial\mathbf{q}}\middle|\Psi^{(v)}_{\mathbf{q}}\right\rangle. \tag{12}$$

Here $\Psi^{(\mathrm{v})}_{\mathbf{q}}$ and $\Psi^{(\mathrm{c})}_{\mathbf{q}}$ are periodic Bloch functions, i.e., eigenfunctions of the Hamiltonian without an optical field; matrix element $\mathcal{A}_{cv}(\mathbf{q})$ is the well-known non-Abelian Berry connection [34–36], and $\phi^{(\mathrm{d})}_{cv}(\mathbf{q}, t)$ is the dynamic phase; the trajectory in the reciprocal space, $\mathbf{k}(\mathbf{q}, t)$, is given by the Bloch theorem (7). Note that the interband dipole matrix element, which determines optical transitions between the VB and the CB at crystal momentum $\mathbf{q}$, is $\mathbf{D}_{cv}(\mathbf{q}) = e\mathcal{A}_{cv}(\mathbf{q})$.

In these terms, we introduce Schrödinger equation in the interaction representation in the adiabatic basis of the Houston functions as

$$i\hbar\frac{\partial B_{\mathbf{q}}(t)}{\partial t} = H'(\mathbf{q}, t)B_{\mathbf{q}}(t), \tag{13}$$

where wave function (vector of state) $B_q(t)$ and Hamiltonian $H'(\mathbf{q}, t)$ are defined as

$$B_{\mathbf{q}}(t) = \begin{bmatrix}\beta_{c\mathbf{q}}(t)\\ \beta_{v\mathbf{q}}(t)\end{bmatrix}, \tag{14}$$

$$H'(\mathbf{q}, t) = -e\mathbf{F}(t)\mathbf{G}(\mathbf{q}, t), \tag{15}$$

$$\mathbf{G}(\mathbf{q}, t) = \begin{bmatrix}0 & \mathcal{D}_{cv}(\mathbf{q}, t)\\ \mathcal{D}^*_{cv}(\mathbf{q}, t) & 0\end{bmatrix}. \tag{16}$$

Schrödinger equation (13) defines a solution for dynamics of the system, whose accuracy is limited by the size of the basis set (i.e., truncation of the Hilbert space of the surface states of the TI). In particular, it contains such phenomenon as band-gap opening in the field of a circularly-polarized pulse. A formal general solution of this equation can be presented in terms of the evolution operator, $\hat{S}(\mathbf{q}, t)$, as

$$B_{\mathbf{q}}(t) = \hat{S}(\mathbf{q}, t)B_{\mathbf{q}}(-\infty), \tag{17}$$

$$\hat{S}(\mathbf{q}, t) = \hat{T}\exp\left[i\int_{-\infty}^{t}\mathbf{G}(\mathbf{q}, t')d\mathbf{k}(\mathbf{q}, t')\right], \tag{18}$$

where $\hat{T}$ is the well-known time-ordering operator [37], and the integral is affected along the Bloch trajectory [Eq. (7)].

We introduce Cartesian components of non-Abelian Berry connection as a vector $\{\mathcal{A}_x(\mathbf{k}), \mathcal{A}_y(\mathbf{k})\} = \boldsymbol{\mathcal{A}}_{cv}(\mathbf{k})$. Substituting the eigenfunctions of the field-free Hamiltonian (1) into Eq. (12), we obtain for its components

$$\mathcal{A}_x(\mathbf{k}) = \mathcal{N}\left(-\frac{1}{2}\frac{k_y}{k^2} - i\frac{2k_x^4 + 3k_y^2\left(k_x^2 - k_y^2\right)}{k^2\sqrt{4k_x^2\left(k_x^2 - 3k_y^2\right)^2 + \left(\frac{A_2}{A_3}k\right)^2}}\right), \tag{19}$$

$$\mathcal{A}_y(\mathbf{k}) = \mathcal{N}\left(\frac{1}{2}\frac{k_x}{k^2} + i\frac{k_xk_y\left(7k_x^2 + 3k_y^2\right)}{k^2\sqrt{4k_x^2\left(k_x^2 - 3k_y^2\right)^2 + \left(\frac{A_2}{A_3}k\right)^2}}\right), \tag{20}$$

where the normalization coefficient is

$$\mathcal{N} = \left(1 + \frac{4k_x^2\left(k_x^2 - 3k_y^2\right)^2}{\left(\frac{A_2}{A_3}k\right)^2}\right)^{-\frac{1}{2}}.$$

Similar to graphene, there are singularities at the Dirac point, $\mathbf{k} = 0$, for both $\mathcal{A}_x(\mathbf{k})$ and $\mathcal{A}_y(\mathbf{k})$—see Fig. 2. However, unlike graphene, $\mathcal{A}_x(\mathbf{k})$ and $\mathcal{A}_y(\mathbf{k})$ have both imaginary and real parts due to the warping term in the surface Hamiltonian (1). Consequently, there is a nontrivial dependence on angle, $\tan^{-1}(k_y/k_x)$: The components of the non-Abelian Berry connection, $\mathcal{A}_x$ and $\mathcal{A}_y$, exhibit sharp maxima along six and four ridges, which are clearly seen in Figs. 2(a) and 2(c), respectively.

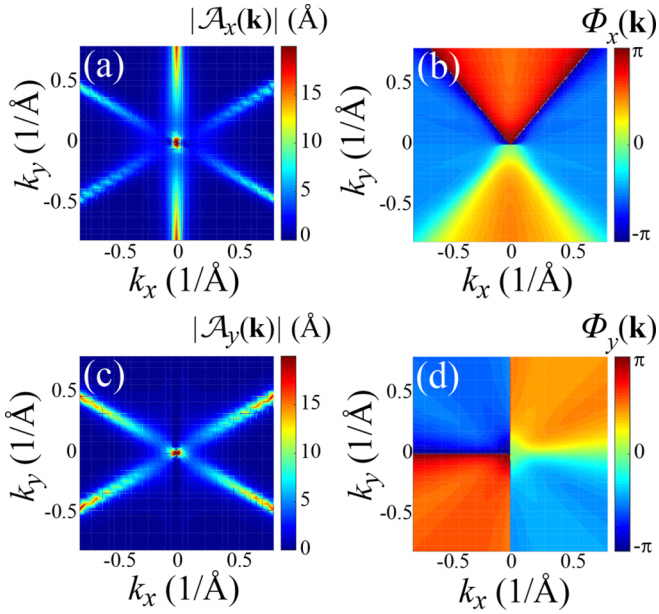

FIG. 2. Complex vector of non-Abelian Berry connection $\boldsymbol{\mathcal{A}} = \boldsymbol{\mathcal{A}}_{cv}$. (a) Magnitude of x-component $|\mathcal{A}_x(\mathbf{k})|$ (in units of Å) as a function of crystal momentum $\mathbf{k}$. (b) Phase $\Phi_x(\mathbf{k}) = \arg(\mathcal{A}_x(\mathbf{k}))$ as a function of crystal momentum $\mathbf{k}$. (c) Same as (a) but for $\mathcal{A}_y(\mathbf{k})$. (d) Same as (b) but for $\Phi_y(\mathbf{k}) = \arg(\mathcal{A}_y(\mathbf{k}))$.

When an electron is compelled by the optical field to move within a band, the transitions will occur when its trajectory $\mathbf{k}(\mathbf{q}, t)$, which is defined by the Bloch acceleration theorem (7)], crosses these ridges and passes in the vicinity of the Dirac point. The corresponding transition amplitudes will interfere generating a texture of fringes in the reciprocal space.

We solve Eq. (13) numerically with an initial condition corresponding to an occupied VB and an empty CB [$\beta_{v\mathbf{q}}(-\infty) = 1$ and $\beta_{c\mathbf{q}}(-\infty) = 0$]. As a result. we obtain the occupation amplitudes of the VB and CB as functions of time, $\beta_{v\mathbf{q}}(t)$ and $\beta_{c\mathbf{q}}(t)$. At each moment of time, they satisfy the normalization condition

$$|\beta_{v\mathbf{q}}(t)|^2 + |\beta_{c\mathbf{q}}(t)|^2 = 1\,. \tag{21}$$

We introduce residual population probabilities of the valence and conduction bands as a function of crystal momentum as

$$N_{\mathrm{VB}}^{(\mathrm{res})}(\mathbf{q}) = |\beta_{v\mathbf{q}}(t=\infty)|^2,\ N_{\mathrm{CB}}^{(\mathrm{res})}(\mathbf{q}) = |\beta_{c\mathbf{q}}(t=\infty)|^2\,, \tag{22}$$

and the mean residual CB population probability as

$$n_c = \frac{1}{N}\sum_{\mathbf{q}\in\mathrm{BZ}} N_{\mathrm{CB}}^{(\mathrm{res})}(\mathbf{q})\,, \tag{23}$$

where N is the total number of electrons per unit cell, and the summation over the crystal momentum in the first Brillouin zone (BZ) is conventionally defined as

$$\sum_{\mathbf{q}\in\mathrm{BZ}}(\dots) = A\int_{\mathrm{BZ}}(\dots)\frac{d^2k}{(2\pi)^2}\,, \tag{24}$$

and A is the area of the (real-space) unit cell. For an electroneutral system where the Fermi energy is at the Dirac point,

$$A\int_{\mathrm{BZ}}\frac{d^2k}{(2\pi)^2} = N\,, \tag{25}$$

so n_c is a positive dimensionless number between 0 and 1, as should be for the mean probability. The mean residual density of the CB electrons is Nn_c/A. Note that in the absence of the spin-momentum locking, a quantity in the right-hand side of Eq. (25) would be $N/2$.

Compare results for 3D TI with the corresponding results for graphene where the low-energy Dirac Hamiltonian is

$$H_0^{(\mathrm{gr})} = \hbar v_F(\sigma_x k_x + \sigma_y k_y), \tag{26}$$

where $v_F \sim 10^6$ m/s is the Fermi velocity. Then the energies of the CB and VB are

$$\begin{aligned} E_c^{(\mathrm{gr})}(\mathbf{k}) &= \hbar v_F k \\ E_v^{(\mathrm{gr})}(\mathbf{k}) &= -\hbar v_F k\,. \end{aligned} \tag{27}$$

The corresponding components of the non-Abelian Berry connection for graphene are

$$\mathcal{A}_x^{(\mathrm{gr})}(\mathbf{k}) = \frac{-\frac{1}{2}k_y}{k_x^2+k_y^2}\,, \tag{28}$$

$$\mathcal{A}_y^{(\mathrm{gr})}(\mathbf{k}) = \frac{\frac{1}{2}k_x}{k_x^2+k_y^2}\,. \tag{29}$$

These are obviously real quantities in contrast to Eqs. (19) and (20).

III. RESULTS AND DISCUSSION

A. Linearly polarized pulse

We apply a linearly-polarized single-oscillation optical pulse incident normally to the surface of 3D TI. The electric field waveform of the pulse in the surface plane of the TI is parametrized in the following form

$$\mathbf{F}(t) = \{F_x(t), F_y(t)\} = F(t)\{\cos(\theta), \sin(\theta\}), \tag{30}$$

where $F(t) = F_0 e^{-u^2}(1-2u^2)$, F_0 is the amplitude of the field, $u = t/\tau$, τ is (on the order of magnitude) a half duration of the optical oscillation (in calculations, we choose $\tau = 1$ fs), and θ is the polarization angle of the applied field. Before the pulse, the CB is empty, and the VB is fully occupied. During the pulse, the electron dynamics is characterized by redistribution of electrons between the VB and the CB. After the pulse, there is a significant residual CB population—see Fig. 3—manifesting irreversibility related to the gapless spectrum of the TI's surface states. Note that an earlier work [28,38,39] showed that strong-field induced CB population is highly reversible, i.e., disappearing after the pulse end, for insulators such as silica and alumina (quartz and sapphire). This reversibility is due to the presence of a wide band gap (≈10 eV) between the VB and the CB, which significantly exceeds the characteristic frequency of the excitation pulse. Such a condition causes the CB population to adiabatically follow the magnitude (modulus) of the pulse field, $|F(t)|$. This is not the case for TI's since their surface-band spectrum is gapless.

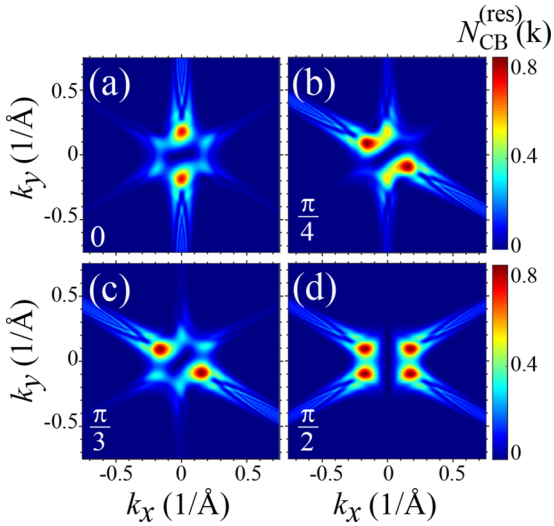

FIG. 3. Residual CB population, $N^{(res)}$, on the surface of Bi_2Se_3 as a function of wave vector $\mathbf{k}$ for different values of angle θ. Amplitude of the electric field is $F_0 = 0.10$ V/Å. The angle is (a) $\theta = 0$, (b) $\theta = \pi/4$, (c) $\theta = \pi/3$, and (d) $\theta = \pi/2$.

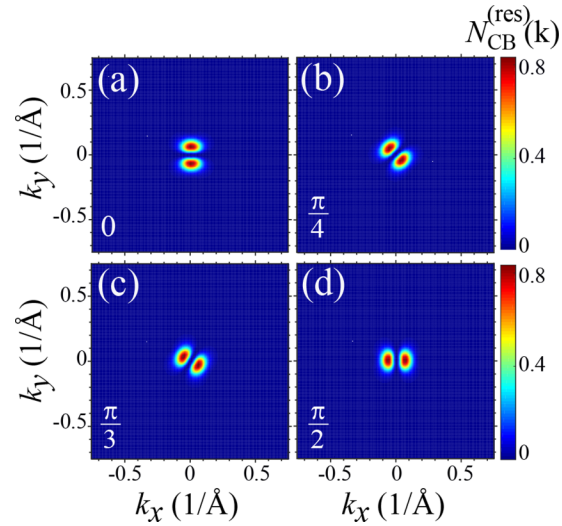

FIG. 4. Residual CB population, $N_{CB}^{(res)}$, of graphene as a function of wave vector $\mathbf{k}$ for different values of angle θ. Amplitude of the electric field is $F_0 = 0.10$ V/Å. The angle is (a) $\theta = 0$, (b) $\theta = \pi/4$, (c) $\theta = \pi/3$, and (d) $\theta = \pi/2$. The dynamics of the graphene system is modeled within the low energy effective Dirac model.

The distribution of the residual CB population in the first Brillouin zone of the surface bands of Bi_2Se_3 is shown in Fig. 3 for different angles between the polarization direction and the positive x axis: (a) $\theta = 0$, (b) $\theta = \pi/4$, (c) $\theta = \pi/3$, and (d) $\theta = \pi/2$. The amplitude of the electric field is $F_0 = 0.1$ V/Å. There is a pattern of "hot spots" with a large CB population and with adjacent interference fringes that are clearly visible. The pair of hot spots seen in each panel is an image of the Dirac point split by a dark line passing through the Γ point in the polarization direction. Note that this dark line originates from electrons passing twice through the Dirac point, which results in their return back to the VB and the zero CB population. This can also be interpreted as a result of the pseudospin conservation. The interference fringes farther from the Dirac point in Figs. 3(a)–3(c) show a pronounced chirality. These fringes originate from the electron VB → CB transitions caused the warping term in the Hamiltonian and replicate its symmetry.

Note that somewhat similar electron distributions have been predicted by us for crystalline TI's [40]. There is also an interference pattern predicted, which consists of the two hot spots originating from the M-point and peripheral interference fringes caused by quadratic terms in the Hamiltonian.

The components of the non-Abelian Berry connection, which are responsible for the interband coupling for a given direction of polarization, are $\mathcal{A}_x(\mathbf{k})$ and $\mathcal{A}_y(\mathbf{k})$ for $\theta = 0$ and $\theta = \pi/2$, respectively, cf. Fig. 2. The distribution of $N_{CB}^{(res)}(\mathbf{k})$ reflects the profile of the corresponding components, $\mathcal{A}_x(\mathbf{k})$ and $\mathcal{A}_y(\mathbf{k})$, see Figs. 3(a) and 3(d), respectively.

This behavior of the residual CB population is somewhat similar to but also possesses significant differences from what is calculated for graphene near the Dirac points (K or K'), see Fig. 4, where the residual CB population is shown for a low-energy effective model of graphene [Eq. (26)] for different polarization directions. The distribution of $N_{CB}^{(res)}(k)$ for graphene is symmetric with respect to the polarization plane in contrast to the 3D TI, cf. Fig. 3, where this symmetry is broken by the warping term.

There is also another fundamental physical difference between the electron-distribution textures in graphene and TI. In the Dirac approximation, there is locking of crystal momentum and pseudospin in graphene, and this locking is opposite in the VB and CB. For TIs, there is locking of crystal momentum and real electron spin, which is also opposite for the VB and the CB. Such locking is valid in the Dirac approximation, which is applicable close enough to the Γ point. Thus the textures of the electron population in the reciprocal space are simultaneously spin-polarization textures. Potentially, such momentum/spin textures can be directly measured using spin-polarized TR-ARPES [2,41].

The mean residual CB population (averaged over a part of the surface Brillouin zone close to the Dirac point), n_c, as a function of field amplitude, F_0, is shown for the linearly polarized pulse in Fig. 5. This population monotonically increases with F_0 and has only a weak dependence on the direction of polarization. For a given field amplitude, the maximum CB population is realized for the y polarized pulse, $\theta = \pi/2$, while the minimum is at $\theta \approx \pi/8$ (see inset).

B. Circularly polarized pulse

Two-dimensional solids and topological crystals in the reciprocal space possess nontrivial topological properties (chirality) related to the Berry-Zak phase [35,42,43]. In this section, we will study this topology using circularly-polarized ultrashort pulses. These fundamentally promise reacher responses of chiral systems because they probe the system's chirality with their own chirality.

A one-cycle circularly-polarized pulse we will use has electric field that can be parametrized as the following

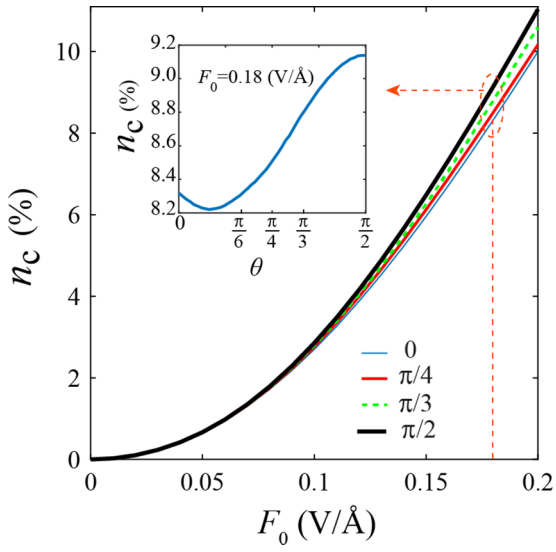

FIG. 5. Mean residual CB population n_c as a function of field amplitude F_0 for different values of θ: $\theta = 0$ (blue solid line), $\theta = \pi/4$ (red solid line), $\theta = \pi/3$ (green dashed line), and $\theta = \pi/2$ (black solid line). Inset: total residual CB population, n_c, as a function of θ for the amplitude of the electric field of $F_0 = 0.18$ V/Å.

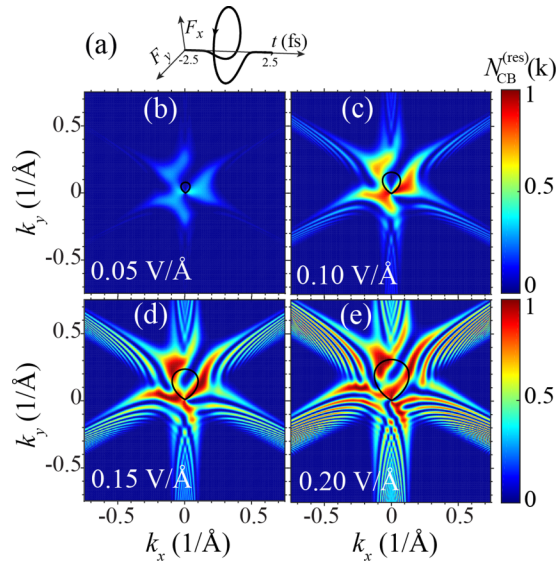

FIG. 6. Residual CB population as a function of crystal momentum. Excitation pulse is right-handed circularly polarized; its waveform is shown in panel (a). The amplitude of the pulse is (b) $F_0 = 0.05$ V/Å, (c) $F_0 = 0.10$ V/Å, (d) $F_0 = 0.15$ V/Å, and (e) $F_0 = 0.20$ V/Å. The solid closed black lines display the separatrices (see the text) for the corresponding pulses.

waveform:

$$\mathbf{F}(t) = \{F_x(t), F_y(t)\},$$
$$F_x(t) = \pm F_0 e^{-u^2}(1 - 2u^2),$$
$$F_y(t) = 2F_0 u e^{-u^2}, \tag{31}$$

where sign $\pm$ determines the handedness of the pulse [+ is for a right-hand circularly polarized pulse (RCP), and − is for a left-hand circularly polarized pulse (LCP)]. For brevity, we denote such one-cycle RCP as 1R and one-cycle LCP as 1L. These 1R and 1L pulses are related by reflection in the yz plane ($\mathcal{P}_{yz}$ reflection). Note that the same change of handedness can be obtained by $\mathcal{T}$ reversal plus reflection in the coordinate center, i.e., $\mathcal{T}\mathcal{P}_{yz}\mathcal{P}_{xz}$ transformation. The pairs of pulses with opposite chirality are ideally suited to probe the chirality of the surface Bloch bands because the resulting electron distributions depend on the sign of the Berry curvature with respect to the pulse chirality.

Following this line, for a 1R pulse, residual CB population distributions in the reciprocal space are shown in Fig. 6 for several field amplitudes F_0. Similar to the linear-polarization case considered above in Sec. III A, here the residual CB population is also large for $F_0 \gtrsim 0.1$ V/Å implying that the electron dynamics is highly irreversible. The CB population distribution shows a chiral pattern, which is correlated with the handedness of the pulse.

A solid closed black curve seen in Figs. 6(b)–6(e) is the separatrix [12]. This is defined as a set of initial points $\mathbf{q}$ for which electron trajectories pass precisely through the Dirac (Γ) point. Its parametric equation is $\mathbf{q}(t) = -\mathbf{k}(0, t)$, where $t \in (-\infty, \infty)$ is a parameter, and $\mathbf{k}(\mathbf{q}, t)$ is a Bloch trajectory originating at a point $\mathbf{q}$ as given by Eq. (7). Thus, the separatrix is an electron trajectory starting at $\mathbf{k} = 0$ (i.e., at the Γ point) and reflected in the xz plane ($\mathcal{P}_{xz}$ reflection). For initial crystal momentum $\mathbf{q}$ inside of the separatrix, the electron trajectory, $\mathbf{k}(\mathbf{q}, t)$, encircles the Γ point, otherwise it does not.

Because the coupling dipole matrix element (the non-Abelian Berry connection) is large (singular) at the Γ point [see Fig. 2], one may expect that the residual CB population will be enhanced close to the separatrix. This was the case for graphene in Ref. [12] (see also Fig. 7 and its discussion below in this section) but it is not pronounced in the present study, as Fig. 6 demonstrates.

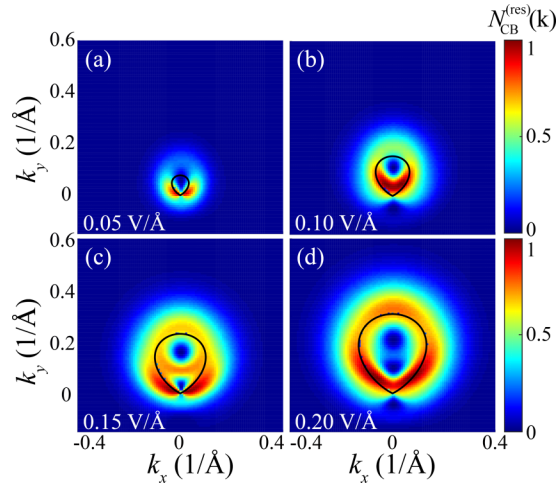

FIG. 7. Residual CB population in the vicinity of a Dirac point for graphene for circularly-polarized right-handed one-cycle pulse with amplitude of (a) $F_0 = 0.05$ V/Å, (b) $F_0 = 0.10$ V/Å, (c) $F_0 = 0.15$ V/Å, and (d) $F_0 = 0.20$ V/Å. The solid closed black lines display the separatrices (see the text) for the corresponding pulses.

A fundamental difference between the TI and graphene is that the non-Abelian Berry curvature, $\mathbf{\Omega}_{cv}(\mathbf{k}) = \frac{\partial}{\partial \mathbf{k}} \times \boldsymbol{\mathcal{A}}_{cv}(\mathbf{k})$, a gauge-invariant field whose integral over reciprocal space area is equal to the Berry phase, for graphene is real and singular—it has a δ-function singularity localized at the Dirac (K and K') points. For a circular pulse for graphene, there is only one passage of an electron, which is moving in the reciprocal space, by the Dirac point. Thus there is only one significant amplitude to undergo a VB $\rightarrow$ CB transition, and, consequently, there is no pronounced interference along the separatrix, see Fig. 7. Note that these illustrative data for graphene were calculated as in Ref. [12].

In a sharp contrast, in the present model of TI, there are regions along the radial lines emanating from the Γ point, which are seen as ridges in Fig. 2, where the non-Abelian Berry connection (dipole matrix element) is increased and possesses a nontrivial phase. These regions overlap in the vicinity of the Γ point close to the separatrix. Consequently, the corresponding amplitudes of the VB $\rightarrow$ CB transitions interfere causing the chiral pattern of interference fringes seen in Fig. 6. The separatrix itself is surrounded by regions of high CB population but not seen as a continuous arc in contrast to the case of graphene—cf. Fig. 7 and Ref. [12].

For high enough fields, $F_0 \gtrsim 0.1$ V/Å, there is a pronounced pattern of interference fringes in Figs. 6(b)–6(e). Note that this pattern is a self-referenced electron interferrogram whose chirality is due to the nontrivial phase of the non-Abelian Berry connection. This interference is caused by passing a ridge of $\mathcal{A}$ twice during one optical cycle and, also, additionally by passing close to the Dirac point where the VB $\rightarrow$ CB transitions predominantly occur. The corresponding transition amplitudes interfere generating the fringes, which carry information about both the non-Abelian Berry curvature and the dynamic phase.

The CB population for the left-handed pulse (1L) is shown in Fig. 8. Obviously it is related to the pattern in Fig. 6 by the $\mathcal{P}_{yz}$ reflection. This is exactly as expected from the symmetry of the problem. Correspondingly, the distributions in Fig. 8 exhibit opposite chiralities but otherwise are similar to those in Fig. 6.

We consider also pulses consisting of two optical cycles with opposite chiralities whose waveforms are parametrized as

$$F_x(t) = F_0\big(e^{-u^2}(1-2u^2) \pm e^{-(u-u_0)^2}(1-2(u-u_0)^2)\big)\,,$$
$$F_y(t) = 2F_0\big(ue^{-u^2} + (u-u_0)e^{-(u-u_0)^2}\big)\,, \qquad (32)$$

where $u_0 = t_0/\tau$ and $\tau = 1$ fs. The delay time (the time between the two cycles) is $t_0 = 4$ fs. Here the plus sign in the above expression corresponds to two right-handed cycles (2R), while the minus sign corresponds to one right-handed cycle followed by one left-handed cycle (1R+1L). Note these opposite-chirality pulses are related by the $\mathcal{P}_{yz}$ reflection instead of the $\mathcal{T}$ reversal.

The residual CB population for the two-cycle pulse is shown in Fig. 9(a) for the 2R pulse and Fig. 9(b) for the 1R+1L pulse. In comparison to the corresponding one-cycle 1R pulse [Fig. 6(c)], the CB population for two-cycle pulses

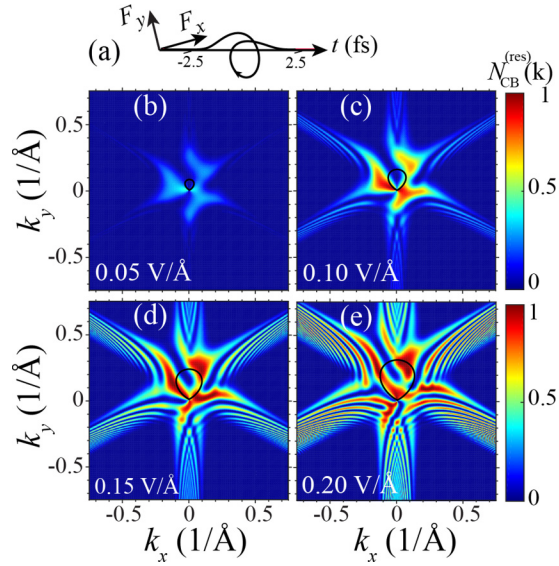

FIG. 8. Residual CB population for circularly-polarized left-handed one-cycle pulse [waveform is shown on panel (a)] with amplitude of (b) $F_0 = 0.05$ V/Å, (c) $F_0 = 0.10$ V/Å, (d) $F_0 = 0.15$ V/Å, and (e) $F_0 = 0.20$ V/Å. The solid closed black lines display the separatrices (see the text) for the corresponding pulses.

shows more interference fringes, which is due to the interference of the transition amplitudes accumulated during the two constituent subcycles. The CB population distribution also has a chiral pattern for all types of two-cycle pulses (2R and 1R+1L). This chirality is due to non-Abelian Berry phase, which is nonzero due to the warping terms in the Hamiltonian of Eq. (1). In a sharp contrast, in graphene the non-Abelian Berry connection is real—see Eqs. (28) and (29). Consequently, the residual CB population for any pulses of the same chirality (1R, 1L, 2R, or 2L) is nonchiral and symmetric with respect to the $\mathcal{P}_{yz}$ reflection [12].

There is an interesting analogy of the two-cycle chiral pulse discussed above in the previous paragraph and periodic circularly-polarized excitation studied in Ref. [6]. The latter shows a pattern of repeated Floquet-Bloch bands separated by the characteristic excitation frequency $\sim\bar{\omega}$. Though our pulse is strictly speaking aperiodic, for the case of two subpulses, there is a sense of repetition with frequency $\bar{\omega}$. In fact, in

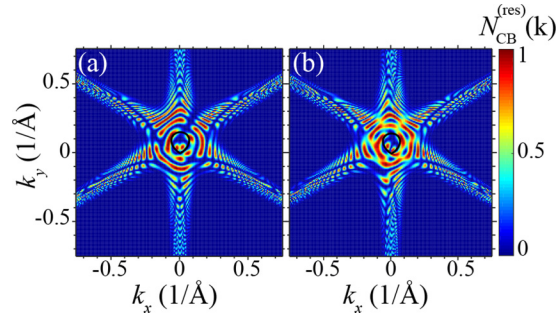

FIG. 9. Residual CB population for two-cycle circularly polarized pulse with the amplitude of 0.1 V/Å. The two-cycle pulses are 2R (a) and 1R+1L (b). The solid closed black lines display the separatrices (see the text).

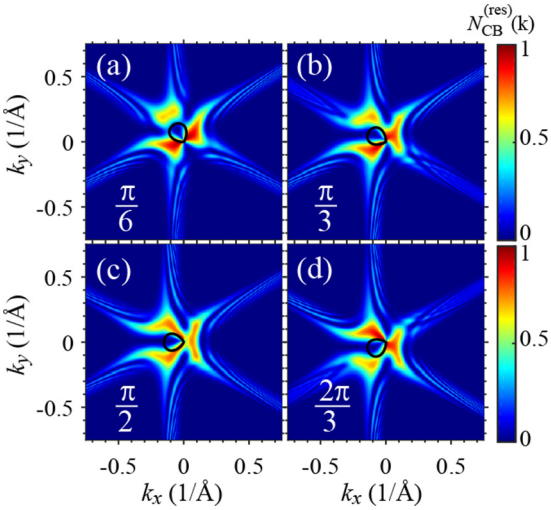

FIG. 10. Residual electron population after 1R single-oscillation pulse with amplitude $F_0 = 0.1$ V/Å. The corresponding carrier-envelope phase (i.e., the angle between the maximum field, F_0, and the positive x axis) is indicated in the corresponding panels.

Fig. 9, there is a repeated pattern of interference fringes separated by a crystal momentum $\Delta k \sim \bar{\omega}/v_F$; this separation is proportional to the mean excitation frequency $\bar{\omega}$ and does not depend on field amplitude just like for quasienergies in the Floquet-Bloch picture of Ref. [6]. Moreover, the energy separation between the fringes, $\Delta E \sim \hbar v_F \Delta k \sim \hbar\bar{\omega}$ is the same on the order of magnitude as the separation of the Floquet-Bloch bands.

As we have already discussed above in conjunction with Eqs. (19) and (20), for the TI's surface reciprocal space, the Berry curvature is distributed (not localized) bringing about a nontrivial phase that leads to chirality of the CB residual electron distribution. In Figs. 10(a)–10(d) [see also Fig. 6(c) for comparison], we illustrate the dependence of this chirality on the orientation of the 1R pulses for a moderate pulse amplitude, $F_0 = 0.1$ V/Å. Note that this orientation is determined by the angle between the direction of the maximum field, $\mathbf{F}_0$, and the positive x axis, which is nothing else as the carrier-envelope phase, θ, of the pulse. As we see from these figures, the chirality is present for $\theta = 0, \pi/3$, and $2\pi/3$; it is completely absent for $\theta = \pi/6$ (a reflection symmetry plane is at $\theta = 2\pi/3$) and $\theta = \pi/2$ (the symmetry plane is at $\theta = 0$). Generally, the chirality is absent when the maximum field is in the direction of any of the ridges in Fig. 2(a), i.e., $\theta = \frac{\pi}{6} + n\frac{\pi}{3}$, where n is an integer; in such a case there is a symmetry plane normal to the direction of the ridge. In contrast, the chirality is maximum when the maximum field is along the bisector between the ridges, $\theta = n\frac{\pi}{3}$.

Note that in all cases of Fig. 6(c) and Figs. 10(a)–10(d), the electron distribution consists of "bright" regions of a high population adjacent to and outside of the separatrix. These bright regions have peripheral "wings" extending along the six ridges of the non-Abelian Berry connection [Fig. 2(a)] $\boldsymbol{\mathcal{A}}_{cv}(\mathbf{k})$.

Optical pulses, both linearly and circularly polarized, create generally asymmetric carrier distributions in the reciprocal space. These will manifest themselves as currents (net charge transfer) in the real space—cf. Refs. [14,38,39]. The corresponding charge transfer per pulse can be measured macroscopically. For linearly polarized pulses, the direction of the net charge transfer is parallel to the maximum electric field. The net charge transferred (sign and magnitude) is defined by the carrier-envelope phase of the pulse and provides a direct access to its measurement [44].

For circularly polarized pulses considered in this paper, the resulting electron distributions in the reciprocal space are generally both asymmetric and chiral. Correspondingly, there are two types of currents: (i) Direct current in a direction parallel to the maximum field and (ii) Hall current in the normal direction. The latter depends on the chirality of the pulse vs the chirality of the Bloch bands at the Γ point. There is a circular current present during the pulse that follows the boundary of the TI's surface. This current will produce THz radiation as in Ref. [45], which can also provide an access to the ultrafast electron dynamics.

We will publish our detailed quantitative results on the photocurrents induced in TI's elsewhere. Below in this section, we only provide an expression for the intraband current and its order-of-magnitude estimate. The current induced by the pulse has two components: interband current $\mathbf{j}^{(\mathrm{inter})}$ and intraband current $\mathbf{j}^{(\mathrm{intra})}$, which are time derivatives of the corresponding components of the dielectric polarization, $\mathbf{j} = \partial\mathbf{P}/\partial t$. After the pulse, the interband current rapidly decays due to dephasing (Landau damping) while the intraband current is ballistic: It persists longer decaying only due to collisions. Here we only consider the intraband current for the period just after the end of the excitation when the collisions have not yet dissipated it. Two-dimensional density of current is given by an evident expression

$$\mathbf{j}^{(\mathrm{intra})} = \frac{e}{A}\sum_{\mathbf{q}\in\mathrm{BZ}} N_{\mathrm{CB}}^{(\mathrm{res})}(\mathbf{q})\left[\mathbf{v}_c^{(\mathrm{g})}(\mathbf{q}) - \mathbf{v}_v^{(\mathrm{g})}(\mathbf{q})\right], \tag{33}$$

where $\mathbf{v}_\alpha^{(\mathrm{g})}(\mathbf{q}) = \partial E_\alpha(\mathbf{q})/\partial\mathbf{q}$ is the electron group velocity in the corresponding band $\alpha = c, v$. Note that the dimensionality of $\mathbf{j}^{(\mathrm{intra})}$ is A/m.

Taking into account that $\mathbf{v}_c^{(\mathrm{g})} \approx -\mathbf{v}_v^{(\mathrm{g})}$, the CB and the VB give approximately equal contributions to the current. Thus an order-of-magnitude estimate of this current density is

$$j^{(\mathrm{intra})} \sim 2\frac{e}{A} v_c^{(\mathrm{g})} N n_c \epsilon_c\,, \tag{34}$$

where ϵ_c is an asymmetry factor of the electron CB distribution (the symmetric part of this distribution does not contribute to the current),

$$\epsilon_c = \frac{1}{n_c N}\sum_{\mathbf{q}\in\mathrm{BZ}} N_{CB}^{(\mathrm{res})}(\mathbf{q})\frac{\mathbf{v}_c^{(\mathrm{g})}(\mathbf{q})}{\left|\mathbf{v}_c^{(\mathrm{g})}(\mathbf{q})\right|}\,. \tag{35}$$

Fot the sake of estimate, we set $n_c = 0.04$ and $\epsilon_c = 0.1$ (these calculated for $F_0 = 0.1$ V/Å), $N = 1$, and $v_c^{(\mathrm{g})} \sim 10^6$ m/s (as for graphene), and $A \sim (4\ \text{Å})^2$ (assuming typical dimensions of the unit cell). From this and Eq. (34), we obtain

$$j^{(\mathrm{intra})} \sim 0.01\ \frac{\mathrm{A}}{\mu\mathrm{m}}\,. \tag{36}$$

This predicted current is relatively large and should present no fundamental problem to measure experimentally. In fact,

much smaller currents were successfully recorded in relevant experiments on graphene [14], and comparable currents were measured in experiments on quartz, sapphire, and calcium fluoride [38,39].

IV. CONCLUSION DISCUSSION

Electron dynamics on the surface of Bi_2Se_3 in the field of an ultrashort and strong optical pulse results in a significant CB population during the pulse, which also persists after the pulse. This residual CB population is large and comparable to the maximum CB population during the pulse, which implies that the electron dynamics is highly irreversible, which is due to the gapless spectrum of the surface Bloch bands. For a linearly polarized pulse, the electron dynamics significantly depends on the polarization direction of the pulse. There is a pattern of interference fringes ("hot spots") in electron CB distributions (see Fig. 3). These fringes appear as a result of interference of two events of the electron passage by the Dirac (Γ) point during the single optical oscillation. These are somewhat similar to those predicted earlier for graphene [11] (the present field is relatively low and only one pair of fringes appear, see Fig. 4). In the TI's, in a contrast to graphene, there are also peripheral fringes caused by the warping term in the Hamiltonian—see Fig. 3. Note that limited preliminary results on linear-polarized pulses interacting with TI's, which included only Fig. 3 of the present paper, were recently published in Conference Proceedings [46].

A circularly-polarized (chiral) single-oscillation pulse induces a chiral distribution of the residual CB population in the reciprocal space. The handedness of the induced chirality is determined by the handedness (right or left) of the pulse. Such a chiral response in Bi_2Se_3 is due to the warping terms in the low-energy surface Hamiltonian near the Dirac (Γ) point. This leads to the non-Abelian Berry connection being complex with phase winding that causes the aforementioned chirality. In a sharp contrast, in graphene the non-Abelian Berry connection is real, and no chirality is induced by a single-oscillation chiral pulse.

The electron interference patterns predicted in this work are self-referenced electron holograms that carry rich information about topological properties (the non-Abelian Berry phase) of the TI reciprocal space and the Bloch band dispersion (dynamic phase). Such self-referenced holograms can be measured using time-resolved angle-resolved photoelectron spectroscopy (TR-ARPES) [8,15]. In principle, it may be possible to restore the topology of the Bloch bands from these holograms. We will consider this problem elsewhere.

In this paper, we have considered electron transitions between and the residual electron population of the surface Bloch bands of TI's. In these Bloch bands, the direction of the spin, in a certain approximation, is locked to the crystal momentum. As has been established both theoretically and experimentally, a momentum-spin texture also is present for the photoelectrons emitted into the free space in the process of ARPES [7,47–51]. However, this free-space texture is generally different from that present in the crystal Bloch bands; it is controlled both by polarization and by energy of the ultraviolet (UV) or extreme ultraviolet (XUV) radiation that causes the photoelectron emission [7,47–51]. Interestingly enough, in our case the UV or XUV pulses should also be ultrafast and, therefore, their spectral band is wide. It is not known currently how such a large bandwidth will affect the spin textures of the emitted electrons. This is a separate problem that we intend to address elsewhere.

ACKNOWLEDGMENTS

The work by M.I.S. was supported by Grant No. DE-FG02-01ER15213 from the Atomic, Molecular and Optical Sciences Program, Office of Basic Energy Sciences, the U.S. Department of Energy. Work of V.A. was supported by Grant No. DE-SC0007043 from the Physical Behavior of Materials Program, Office of Basic Energy Sciences the U.S. Department of Energy. S.A.O.M. gratefully acknowledges support by MURI Grant No. FA9550-15-1-0037 from the U.S. Air Force Office of Scientific Research. J.S.W. support came from EFRI NewLAW Grant No. EFMA-17 41691 from U.S. National Science Foundation.

[1] L. Fu, C. L. Kane, and E. J. Mele, Topological Insulators in Three Dimensions, Phys. Rev. Lett. **98**, 106803 (2007).

[2] D. Hsieh, Y. Xia, L. Wray, D. Qian, A. Pal, J. H. Dil, J. Osterwalder, F. Meier, G. Bihlmayer, C. L. Kane, Y. S. Hor, R. J. Cava, and M. Z. Hasan, Observation of unconventional quantum spin textures in topological insulators, Science **323**, 919 (2009).

[3] M. Z. Hasan and C. L. Kane, *Colloquium* : Topological insulators, Rev. Mod. Phys. **82**, 3045 (2010).

[4] A. Bansil, H. Lin, and T. Das, Colloquium: Topological band theory, Rev. Mod. Phys. **88**, 021004 (2016).

[5] Y. H. Wang, D. Hsieh, D. Pilon, L. Fu, D. R. Gardner, Y. S. Lee, and N. Gedik, Observation of a Warped Helical Spin Texture in Bi_2Se_3 from Circular Dichroism Angle-Resolved Photo-xbrk emission Spectroscopy, Phys. Rev. Lett. **107**, 207602 (2011).

[6] Y. H. Wang, H. Steinberg, P. Jarillo-Herrero, and N. Gedik, Observation of Floquet-Bloch states on the surface of a topological insulator, Science **342**, 453 (2013).

[7] J. Sanchez-Barriga, A. Varykhalov, J. Braun, S. Y. Xu, N. Alidoust, O. Kornilov, J. Minar, K. Hummer, G. Springholz, G. Bauer, R. Schumann, L. V. Yashina, H. Ebert, M. Z. Hasan, and O. Rader, Photoemission of Bi_2Se_3 with Circularly Polarized Light: Probe of Spin Polarization or Means for Spin Manipulation? Phys. Rev. X **4**, 011046 (2014).

[8] I. Gierz, J. C. Petersen, M. Mitrano, C. Cacho, I. C. Turcu, E. Springate, A. Stohr, A. Kohler, U. Starke, and A. Cavalleri, Snapshots of non-equilibrium Dirac carrier distributions in graphene, Nat. Mater. **12**, 1119 (2013).

[9] D. Brida, A. Tomadin, C. Manzoni, Y. J. Kim, A. Lombardo, S. Milana, R. R. Nair, K. S. Novoselov, A. C. Ferrari,

G. Cerullo, and M. Polini, Ultrafast collinear scattering and carrier multiplication in graphene, Nat. Commun. **4**, 1987 (2013).

[10] M. Trushin, A. Grupp, G. Soavi, A. Budweg, D. De Fazio, U. Sassi, A. Lombardo, A. C. Ferrari, W. Belzig, A. Leitenstorfer, and D. Brida, Ultrafast pseudospin dynamics in graphene, Phys. Rev. B **92**, 165429 (2015).

[11] H. K. Kelardeh, V. Apalkov, and M. I. Stockman, Graphene in ultrafast and superstrong laser fields, Phys. Rev. B **91**, 045439 (2015).

[12] H. K. Kelardeh, V. Apalkov, and M. I. Stockman, Attosecond strong-field interferometry in graphene: Chirality, singularity, and Berry phase, Phys. Rev. B **93**, 155434 (2016).

[13] H. Koochaki Kelardeh, V. Apalkov, and M. I. Stockman, Graphene superlattices in strong circularly polarized fields: Chirality, Berry phase, and attosecond dynamics, Phys. Rev. B **96**, 075409 (2017).

[14] T. Higuchi, C. Heide, K. Ullmann, H. B. Weber, and P. Hommelhoff, Light-field-driven currents in graphene, Nature (London) **550**, 224 (2017).

[15] Y. Liu, G. Bian, T. Miller, and T. C. Chiang, Visualizing Electronic Chirality and Berry Phases in Graphene Systems using Photoemission with Circularly Polarized Light, Phys. Rev. Lett. **107**, 166803 (2011).

[16] A. Crepaldi, F. Cilento, B. Ressel, C. Cacho, J. C. Johannsen, M. Zacchigna, H. Berger, Ph. Bugnon, C. Grazioli, I. C. E. Turcu, E. Springate, K. Kern, M. Grioni, and F. Parmigiani, Evidence of reduced surface electron-phonon scattering in the conduction band of Bi_2Se_3 by nonequilibrium ARPES, Phys. Rev. B **88**, 121404 (2013).

[17] A. F. Kemper, M. A. Sentef, B. Moritz, T. P. Devereaux, and J. K. Freericks, Review of the theoretical description of time-resolved angle-resolved photoemission spectroscopy in electron-phonon mediated superconductors, Ann. Phys.-Berlin **529**, 1600235 (2017).

[18] Chao-Xing Liu, Xiao-Liang Qi, HaiJun Zhang, Xi Dai, Zhong Fang, and Shou-Cheng Zhang, Model Hamiltonian for topological insulators, Phys. Rev. B **82**, 045122 (2010).

[19] L. Braun, G. Mussler, A. Hruban, M. Konczykowski, T. Schumann, M. Wolf, M. Münzenberg, L. Perfetti, and T. Kampfrath, Ultrafast photocurrents at the surface of the three-dimensional topological insulator Bi_2Se_3, Nat. Commun. **7**, 13259 (2016).

[20] M. C. Wang, S. Qiao, Z. Jiang, S. N. Luo, and J. Qi, Unraveling Photoinduced Spin Dynamics in the Topological Insulator Bi_2Se_3, Phys. Rev. Lett. **116**, 036601 (2016).

[21] R. J. Cava, Huiwen Ji, M. K. Fuccillo, Q. D. Gibson, and Y. S. Hor, Crystal structure and chemistry of topological insulators, J. Mater. Chem. C **1**, 3176 (2013).

[22] Y. D. Glinka, S. Babakiray, T. A. Johnson, M. B. Holcomb, and D. Lederman, Resonance-type thickness dependence of optical second harmonic generation in thin-films of the topological insulator Bi_2Se_3, Phys. Rev. B **91**, 195307 (2015).

[23] Haijun Zhang, Chao-Xing Liu, Xiao-Liang Qi, Xi Dai, Zhong Fang, and Shou-Cheng Zhang, Topological insulators in Bi_2Se_3, Bi_2Te_3 and Sb_2Te_3 with a single Dirac cone on the surface, Nat. Phys. **5**, 438 (2009).

[24] W. X. Feng and Y. G. Yao, Three-dimensional topological insulators: A review on host materials, Science China-Physics Mechanics Astronomy **55**, 2199 (2012).

[25] Liang Fu, Hexagonal Warping Effects in the Surface States of the Topological Insulator Bi_2Te_3, Phys. Rev. Lett. **103**, 266801 (2009).

[26] P. B. Corkum and F. Krausz, Attosecond science, Nat. Phys. **3**, 381 (2007).

[27] F. Krausz and M. Ivanov, Attosecond physics, Rev. Mod. Phys. **81**, 163 (2009).

[28] Ferenc Krausz and Mark I. Stockman, Attosecond metrology: from electron capture to future signal processing, Nat. Photon. **8**, 205 (2014).

[29] O. V. Kibis, Metal-insulator transition in graphene induced by circularly polarized photons, Phys. Rev. B **81**, 165433 (2010).

[30] K. Kristinsson, O. V. Kibis, S. Morina, and I. A. Shelykh, Control of electronic transport in graphene by electromagnetic dressing, Sci. Rep. **6**, 20082 (2016).

[31] M. Claassen, C. J. Jia, B. Moritz, and T. P. Devereaux, All-optical materials design of chiral edge modes in transition-metal dichalcogenides, Nat. Commun. **7**, 13074 (2016).

[32] F. Bloch, Über die quantenmechanik der elektronen in kristallgittern, Z. Phys. A **52**, 555 (1929).

[33] W. V. Houston, Acceleration of electrons in a crystal lattice, Phys. Rev. **57**, 184 (1940).

[34] F. Wilczek and A. Zee, Appearance of Gauge Structure in Simple Dynamical Systems, Phys. Rev. Lett. **52**, 2111 (1984).

[35] D. Xiao, M.-C. Chang, and Q. Niu, Berry phase effects on electronic properties, Rev. Mod. Phys. **82**, 1959 (2010).

[36] F. Yang and R. B. Liu, Nonlinear optical response induced by non-Abelian Berry curvature in time-reversal-invariant insulators, Phys. Rev. B **90**, 245205 (2014).

[37] A. A. Abrikosov, L. P. Gorkov, and I. E. Dzyaloshinskii, *Methods of Quantum Field Theory in Statistical Physics* (Dover Publications, New York, 1975).

[38] A. Schiffrin, T. Paasch-Colberg, N. Karpowicz, V. Apalkov, D. Gerster, S. Muhlbrandt, M. Korbman, J. Reichert, M. Schultze, S. Holzner, J. V. Barth, R. Kienberger, R. Ernstorfer, V. S. Yakovlev, M. I. Stockman, and F. Krausz, Optical-field-induced current in dielectrics, Nature (London) **493**, 70 (2012).

[39] O. Kwon, T. Paasch-Colberg, V. Apalkov, B.-K. Kim, J.-J. Kim, M. I. Stockman, and D. E. Kim, Semimetallization of dielectrics in strong optical fields, Sci. Rep. **6**, 21272 (2016).

[40] S. A. Oliaei Motlagh, V. Apalkov, and M. I. Stockman, Interaction of crystalline topological insulator with an ultrashort laser pulse, Phys. Rev. B **95**, 085438 (2017).

[41] Z.-H. Pan, E. Vescovo, A. V. Fedorov, D. Gardner, Y. S. Lee, S. Chu, G. D. Gu, and T. Valla, Electronic Structure of the Topological Insulator Bi_2Se_3 using Angle-Resolved Photoemission Spectroscopy: Evidence for a Nearly full Surface Spin Polarization, Phys. Rev. Lett. **106**, 257004 (2011).

[42] M. V. Berry, Quantal phase factors accompanying adiabatic changes, Proc. Royal Soc. London Ser. A **392**, 45 (1984).

[43] J. Zak, Berry's Phase for Energy Bands in Solids, Phys. Rev. Lett. **62**, 2747 (1989).

[44] T. Paasch-Colberg, A. Schiffrin, N. Karpowicz, S. Kruchinin, Saglam Ozge, S. Keiber, O. Razskazovskaya, S. Muhlbrandt, A. Alnaser, M. Kubel, V. Apalkov, D. Gerster, J. Reichert, T. Wittmann, J. V. Barth, M. I. Stockman, R. Ernstorfer, V. S. Yakovlev, R. Kienberger, and F. Krausz, Solid-state light-phase detector, Nat. Photon. **8**, 214 (2014).

[45] F. Langer, C. P. Schmid, S. Schlauderer, M. Gmitra, J. Fabian, P. Nagler, C. Schüller, T. Korn, P. G. Hawkins, J. T. Steiner, U. Huttner, S. W. Koch, M. Kira, and R. Huber, Lightwave valleytronics in a monolayer of tungsten diselenide, Nature (London) **557**, 76 (2018).

[46] S. Azar Oliaei Motlagh, Jhih-Sheng Wu, Vadym Apalkov, and Mark I. Stockman, Ultrafast control of electron dynamics in 3d topological insulator, J. Phys.: Conf. Ser. **906**, 012012 (2017).

[47] C.-H. Park and S. G. Louie, Spin Polarization of Photoelectrons from Topological Insulators, Phys. Rev. Lett. **109**, 097601 (2012).

[48] J. H. Ryoo and C.-H. Park, Spin-conserving and reversing photoemission from the surface states of Bi_2Se_3 and Au (111), Phys. Rev. B **93**, 085419 (2016).

[49] C. Jozwiak, C.-H. Park, K. Gotlieb, C. Hwang, D.-H. Lee, S. G. Louie, J. D. Denlinger, C. R. Rotundu, R. J. Birgeneau, Z. Hussain, and A. Lanzara, Photoelectron spin-flipping and texture manipulation in a topological insulator, Nat. Phys. **9**, 293 (2013).

[50] Z. Xie, S. He, C. Chen, Y. Feng, H. Yi, A. Liang, L. Zhao, D. Mou, J. He, Y. Peng, X. Liu, Y. Liu, G. Liu, X. Dong, L. Yu, J. Zhang, S. Zhang, Z. Wang, F. Zhang, F. Yang, Q. Peng, X. Wang, C. Chen, Z. Xu, and X. J. Zhou, Orbital-selective spin texture and its manipulation in a topological insulator, Nat. Commun. **5**, 3382 (2014).

[51] Z. H. Zhu, C. N. Veenstra, S. Zhdanovich, M. P. Schneider, T. Okuda, K. Miyamoto, S. Y. Zhu, H. Namatame, M. Taniguchi, M. W. Haverkort, I. S. Elfimov, and A. Damascelli, Photoelectron Spin-Polarization Control in the Topological Insulator Bi_2Se_3, Phys. Rev. Lett. **112**, 076802 (2014).